

# Effect of strain, thickness, and local surface environment on electron transport properties of oxygen-terminated copper thin films

Alfonso Sanchez-Soares,<sup>1</sup> Sarah L. T. Jones,<sup>1</sup> John J. Plombon,<sup>2</sup> Ananth P. Kaushik,<sup>2</sup> Roger E. Nagle,<sup>3</sup> James S. Clarke,<sup>2</sup> and James C. Greer<sup>1,\*</sup>

<sup>1</sup>*Tyndall National Institute, University College Cork, Lee Maltings, Dyke Parade, Cork T12 R5CP, Ireland*

<sup>2</sup>*Intel Corporation, Hillsboro, Oregon 97124, USA*

<sup>3</sup>*Intel Ireland, Collinstown, Leixlip, Co. Kildare W23 CX68, Ireland*

(Received 8 June 2016; revised manuscript received 19 August 2016; published 5 October 2016)

Electron transport is studied in surface oxidized single-crystal copper thin films with a thickness of up to 5.6 nm by applying density functional theory and density functional tight binding methods to determine electron transport properties within the ballistic regime. The variation of the electron transmission as a function of film thickness as well as the different contributions to the overall electron transmission as a function of depth into the films is examined. Transmission at the oxidized copper film surfaces is found to be universally low. Films with thickness greater than 2.7 nm exhibit a similar behavior in local transmission per unit area with depth from the film surface; transmission per unit area initially increases rapidly and then plateaus at a depth of approximately 0.35–0.5 nm away from the surface, dependent on surface facet. Unstrained films tend to exhibit a higher transmission per unit area than corresponding films under tensile strain.

DOI: [10.1103/PhysRevB.94.155404](https://doi.org/10.1103/PhysRevB.94.155404)

## I. INTRODUCTION

Understanding the effects of scaling to extreme nanoscale limits of a few nanometers on material properties is required for the design of improved nanoelectronic interconnects and devices. Copper has been chosen as the dominant interconnect material in micro- and nanoelectronics since the decision to replace aluminum for integrated circuit applications that occurred approximately two decades ago. As the size of metallic nanostructures becomes less than the electron mean free path ( $\approx 40$  nm in Cu), significantly more electron collisions with surfaces occur as electrons travel through the sample, which results in a dramatic increase in resistivity. This undesirable increase in line resistance in the nanoscale regime compared to bulk is well established for copper nanostructures [1,2]. Whether copper can function effectively as an interconnect material in future nanoscale devices remains a subject for debate. The role different structural scattering sources such as defects, surfaces, and grain boundaries [3–5] play in determining the overall resistance for specific geometries needs to be understood in order to minimize the line resistance of copper and other proposed materials for nanoelectronics interconnects.

The conductivity of metal thin films is extremely sensitive to processing conditions. In the case of gold thin films, Henriquez *et al.* [6,7] report that electron scattering is governed to a large extent by the grain sizes of the film. When the grain size is much smaller than the electron mean free path, grain boundary scattering becomes critical to resistivity, conversely surface scattering dominates when the grain size is much larger than the electron mean free path. Grain boundary scattering is reported as the most important contributor to scattering in copper thin films with thickness as low as 27 nm [8,9]. The surface environment itself is also known to significantly affect the conductivity of copper thin films. Electron scattering

at the copper-vacuum surface is partially specular, however variations in the surface environment can induce dramatic changes to the conductivity of copper thin films. Scattering at the thin film surface is reported to become diffuse after deposition of Ta [10,11] or surface oxidation [12]. *Ab initio* simulations suggest that scattering at a copper-metal interface is intimately related to the electronic properties of the metals [13]. Resistivity decreases compared to a bare copper surface when the density of states (DOS) of the coating or barrier layer matches that of copper surface atoms (Al and Pd). The converse is also the case with increased resistivity observed for coating metals whose DOS doesn't match copper surface atoms (such as for Ta, Ti, and Ru). However, this resistivity increase on deposition is reported to be reversed by exposure to air, i.e., oxidation of the coating metal for the case of Ta [14]. Zinc coated copper thin films also show reduced surface scattering compared to bare copper surfaces exposed to air [15].

In the following, a theoretical study of electron transport properties in oxidized single-crystal copper thin films using *ab initio* and semiempirical computational techniques is presented. This study explores the effects of different oxidized surface environments, film thickness, and crystallographic orientation along which electronic transport occurs. Consistent with expectations, the transmission at the film surfaces is found to be strongly modulated by the presence of oxygen, and a linear relationship between cross section and transmission for copper films as thin as 2.7 nm is found.

## II. METHOD

### A. Thin film structures

The thin films in this study are based on bulk fcc Cu with two different exposed facets on the surface. The first set of structures have exposed (100) facets at their surfaces in which there is a monolayer of oxidized copper with an oxygen coverage of 0.5 ML, and they present a local

\*jim.greer@tyndall.ie

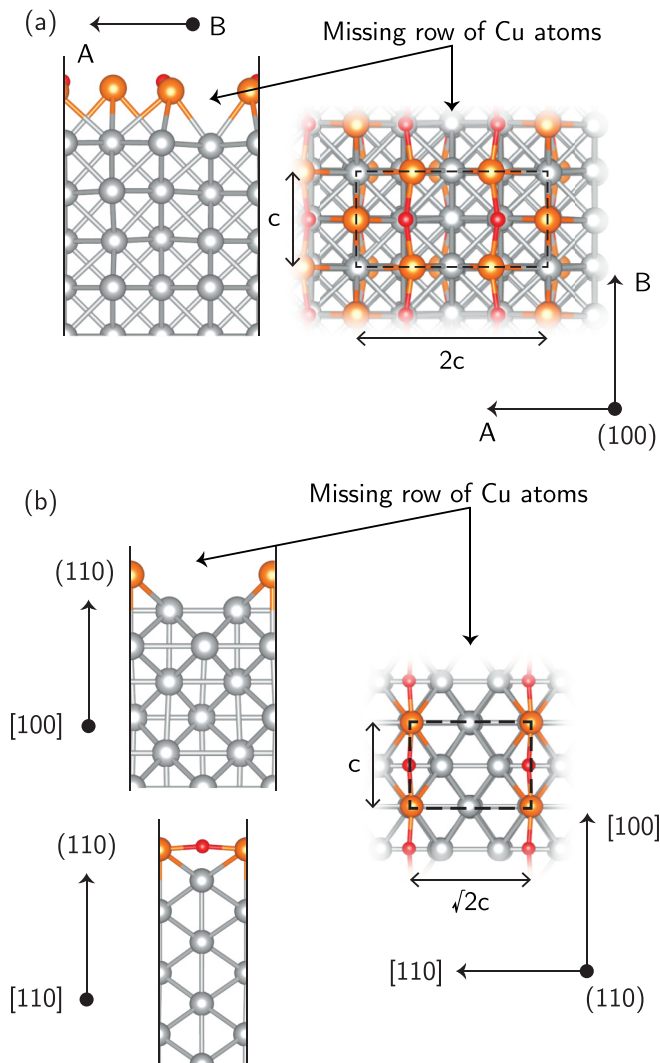


FIG. 1. Side and top view of optimized O-terminated Cu thin films. (a) Cu(100)- $(2\sqrt{2} \times \sqrt{2})R45^\circ$ -O and (b) Cu(110)- $p(2 \times 1)$ -O. Copper atoms away from surfaces are shown in silver.

surface environment with a  $(2\sqrt{2} \times \sqrt{2})R45^\circ$  missing row reconstruction [see Fig. 1(a)], a structure which has previously been theoretically and experimentally identified [16–22]. The immediate surface of the simulated cell consists of 3 Cu atoms and 2 O atoms; each O atom bonds to 4 Cu atoms, three at the surface and one in the Cu layer below the surface, while each surface Cu atom bonds to 2 O atoms. A two-dimensional oxide forms with a missing row of Cu atoms at the surface (as indicated in Fig. 1) with the O atoms inserting into Cu-Cu bonds adjacent to the missing row. This structural rearrangement enables the O-Cu-O angle to be close to  $180^\circ$  as occurs in bulk copper oxides such as CuO and  $\text{Cu}_2\text{O}$ .

Films with thicknesses ranging from 1.9 to 5.6 nm are considered, and in addition the effect of tensile strain on conductance is investigated by studying structures generated with an increased lattice parameter  $c$  from 3.63 Å—the equilibrium lattice parameter within our approximation—to 3.80 Å and 3.90 Å (biaxial strains of 4.7% and 7.4%, respectively). Interconnect copper structures are expected to

present regions with localized strain near interfaces with diffusion barrier layers, which tend to have greater lattice spacings than copper. As dimensions reduce and due to the malleability of metals, the portion of a copper line impacted by strain becomes increasingly important. In the case of ultrathin Cu nanowires, previous work reports a lattice parameter tendency to increase due to the presence of surface oxidation with Cu-Cu spacings increasing as much as 11% [23]. We therefore include the case of tensile strained films in order to assess its impact on the conductivity of copper nanostructures.

Transport along [110] and two perpendicular nonequivalent [100] directions are considered for this set of structures: along axes A and B [see Fig. 1(a)]. Whilst away from the surface both directions are equivalent to [100] in fcc bulk Cu, the surface environment introduces anisotropy: the missing row of Cu atoms is perpendicular to axis A and parallel to axis B.

In order to further explore the effect of different surface environments, a second set of structures with (110) exposed facets, an oxygen coverage of 0.5 ML, and thicknesses ranging from 2.3 to 5.1 nm is studied. In these structures, the surface environment corresponds to the missing row  $p(2 \times 1)$  reconstruction which has been extensively studied [21,24–27], and has been the focus of recent atomic force microscopy studies due to its chemical fingerprinting properties [28–30]. Similar to the previously discussed surface environment, each surface Cu atom bonds to 2 O atoms, while each O atom bonds to 4 Cu atoms: two at the surface and two in the next Cu layer into the film. In these structures, electron transport properties are studied along nonequivalent perpendicular directions which deep into the film correspond to transport along the [100] and [110] crystallographic directions of bulk Cu, respectively [see Fig. 1(b)].

The definition of film thickness is somewhat ambiguous due to the atomistic structure of the films; a convention of choosing the thickness of the slab to be the internuclear separation between atoms in the top and bottom surfaces of the thin film plus twice the atomic radius of Cu (128 pm) is followed.

## B. Computational details

The electronic properties of Cu thin films are studied using density functional theory (DFT) as implemented by the software package OpenMX [31] and density functional tight binding (DFTB) as implemented by QuantumWise [32–34]. The PBE [35] formulation of the generalized gradient approximation (GGA) exchange-correlation functional is used throughout. Norm-conserving pseudopotentials [36] and a strictly localized pseudoatomic orbital (PAO) basis [37,38] are used. The basis sets used are 6.0H-s4p2d2 and 7.0-s2p2 for Cu and O, respectively. The first part of the basis set notation gives the PAO cutoff radius in Bohr, while the second part indicates the orbitals used for the valence electrons, e.g., O 7.0-s2p2 corresponds to a cutoff radius of 7.0 Bohr and 8 basis functions (2 s functions and 6 p functions). Structural parameters derived from this Cu basis set agree well with experiment, giving an optimal fcc lattice parameter of 3.63 Å and a bulk modulus of 135 GPa compared to experimental values of 3.615 Å and 137 GPa, respectively. A supercell approach is taken whereby the thin films are modeled with periodic boundary conditions in the plane of the film and a minimum of 1 nm

of vacuum is introduced in the direction normal to the thin films' surface to prevent interaction of periodic images. The Brillouin zones of the two sets of structures are sampled using a  $11 \times 5 \times 1$  and  $7 \times 9 \times 1$  k-point grid generated according to the Monkhorst-Pack method [39], respectively; and a grid corresponding to an energy cutoff of 200 Ry is used for numeric integration of real-space quantities.

The upper and lower surfaces of the thin films are optimized separately with a frozen bulk Cu back plane as shown in Fig. 1 until forces acting on individual atoms remain below  $3 \times 10^{-4}$  Hartree/Bohr. After optimization of the local surface environment containing the oxide, separate upper and lower surfaces about 0.8 nm thick are joined together and the thickness of the resulting film is increased by the addition of bulklike fcc Cu, with suitable lattice parameter, at the center as required to achieve the desired thickness. The electronic transport properties of the resulting structures are studied in the ballistic transport regime using an approach based on Green's functions [33] within the context of the Landauer-Büttiker formalism [40,41].

The maximum current that can flow through a finite central region connected to two semi-infinite leads is related to the probability of an electron being transmitted through it via the relation

$$I(V) = \frac{e}{h} \sum_{\sigma} \int T_{\sigma}(E, V) \times [f(E, \mu_R, T_R) - f(E, \mu_L, T_L)] dE, \quad (1)$$

where  $e$  is the electron charge,  $h$  is Planck's constant,  $T_{\sigma}(E, V)$  is the transmission coefficient per spin channel  $\sigma$  at energy  $E$  and applied bias  $V$ ,  $f$  is the Fermi-Dirac distribution,  $T_L$  ( $T_R$ ) and  $\mu_L$  ( $\mu_R$ ) are the temperature and chemical potential of the left (right) electrode, and the applied bias is given by

$$V = \frac{\mu_R - \mu_L}{e}. \quad (2)$$

For small applied biases we can approximate the conductance by its linear-response zero-temperature limit in the non-spin-polarized case as

$$G = \frac{2e^2}{h} T(E_F, V = 0). \quad (3)$$

At finite temperatures, the largest contributions to the integral in Eq. (1) will come from the transport of electrons with energies closer to the Fermi level; in particular, assuming slow variations of the transmission coefficients with energy, the previous result can be extended beyond the zero-temperature limit [41].

Throughout this paper, we have computed the transmission coefficients over a 100 meV energy range centered about the Fermi level  $T(E_F \pm 50 \text{ meV}, V = 0)$  as a measure of the films' maximum conductance within the linear-response approximation. This allows an assessment of the variation of transmission coefficients around the Fermi level—and hence the validity of Eq. (3)—and a more robust benchmark of different methods for computing transport properties.

Integration of quantities in electronic transport calculations is performed by sampling with 301 k points along the cell direction parallel to the transmission direction and a single k point along the nonperiodic direction. The computational

demand involved in the calculation of transmission coefficients using first principles DFT becomes prohibitively large as the thickness of the films increase. Therefore we assess the suitability of semiempirical DFTB for calculating electron transmission probabilities in copper nanostructures with oxidized surfaces and under tensile strain. Two sets of DFTB parameters are employed and compared against first principles DFT calculations. The first set of parameters is the matsci set (version 0-3) [42,43] and a second parameter set labeled 'custom,' which has been optimized specifically to have a physical band gap for bulk  $\text{Cu}_2\text{O}$ , which is not reproduced from the matsci parameters.

In the DFTB method [44,45], two center interactions are computed by using Slater-Koster integral tables which describe the Hamiltonian and overlap matrix elements between atoms on an equidistant grid [46]. The 'custom' DFTB parameter set was generated by starting from all-electron DFT wave functions and optimizing interactions between pairs of atoms such that when put into a bulk crystal structure, the experimental band structure of the crystal was recovered. These differ from the matsci parameter set in that specific orbitals and wave functions were targeted to be optimized in order to fit experimental band structures. The procedure followed in their generation is similar to that described by Wahiduzzaman *et al.* [47].

These DFTB calculations also serve as the basis for the determination of transmission pathways [48] within the thin films, which provide a spatially resolved projection of total electron transmission into local coefficients defined between pairs of atoms: For any plane perpendicular to the transmission direction which divides the system in two regions A and B, it holds that

$$T(E) = \sum_{i \in A, j \in B} T_{ij}(E), \quad (4)$$

where  $i$  and  $j$  denote atoms located on each side of said plane. In the case of perfectly periodic systems such as those studied here, the use of a Green's function approach is not necessary in order to obtain the total transmission coefficients at zero applied bias  $T(E, V = 0)$ , but it is required for computing their projection into spatially localized transmission coefficients.

### III. RESULTS AND DISCUSSION

#### A. DFT vs DFTB: Charge transport properties

The DFT calculated total transmission as a function of film thickness and cell parameter  $c$  for directions A and B is shown in Fig. 2. Inspection of the transmission per unit area at the Fermi level reveals a decrease in the maximum current density that can flow through the films with increasing tensile strain (see Table I): As the metal atoms in the structure become further apart and the overlap between their orbitals becomes smaller, the number of conducting paths decreases as it becomes more difficult for electrons to propagate between atoms.

Table I also shows an increase of transmission per unit area at the Fermi level  $\tau(E_F)$  with increasing thickness: The addition of new conducting paths further away from the surface, and hence with a lower associated probability to scatter off it, results in a net increase of the total current density that flows through the thicker films. Figure 3 illustrates these findings by plotting the ratio between the transmission

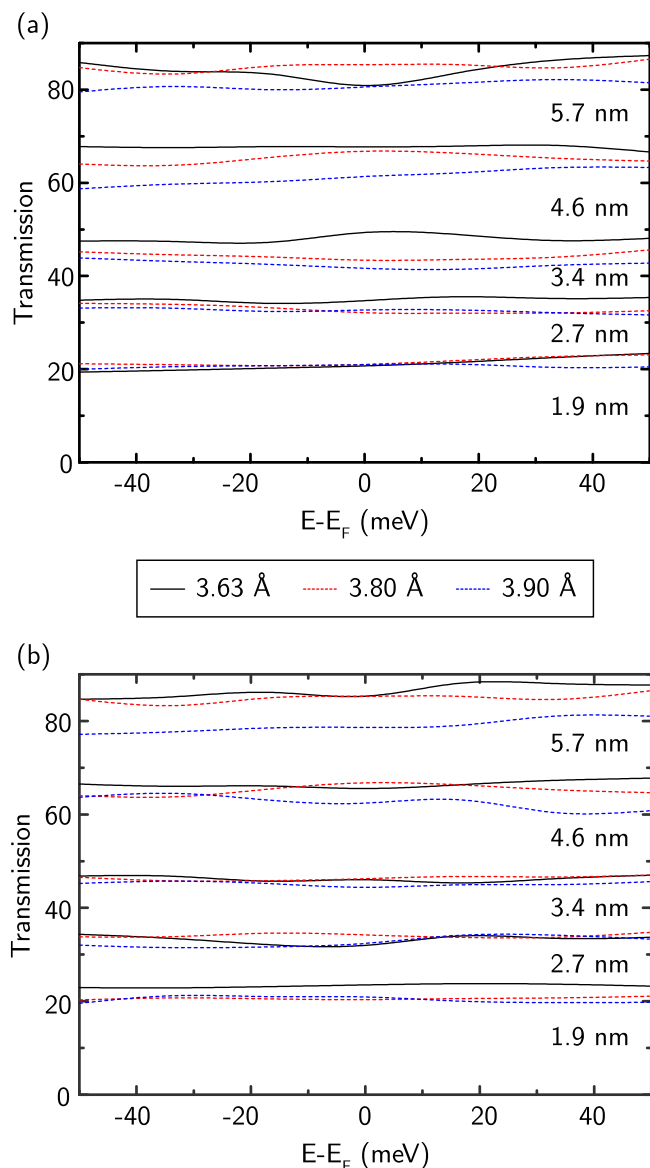


FIG. 2. DFT-computed transmission for film thickness of 2.0, 2.7, 3.4, 4.5, and 5.6 nm with varying values of the lattice parameter  $c$  for inequivalent transport directions (a) A and (b) B as indicated in Fig. 1(a). Zero of energy is taken to be at the Fermi level.

per unit area of the films and that of bulk copper versus film thickness for all considered strains, which is equivalent to the ratio between their conductances.

Similar behavior is observed in DFTB calculations using both parameter sets. Transmission coefficients for all cases shown in Fig. 2 have been computed using both parameter sets. Histograms showing deviations from DFT transmission values at the Fermi level are shown in Fig. 4. The custom parameter set is found to provide a description of the films' electron transport properties closer to that of DFT, with a maximum error of 10% and a standard deviation of 4.4 versus values found for the matsci parameter set of 13% and 6.3, respectively. DFTB hence provides a reasonable approximation for transmission in Cu/O systems at a fraction of the computational cost of DFT and is able to describe thin films under tensile strain

TABLE I. DFT calculated transmission per unit area at  $E_F$  for structures shown in Fig. 1(a) with varying thickness and biaxial tensile strain.

Strain $\rightarrow$	$\tau(E_F)$ ( $\text{nm}^{-2}$ )		
	0 %	4.7%	7.4%
(100)-[100] A			
1.9 nm	7.34	7.08	7.00
2.7 nm	8.99	8.15	8.35
3.4 nm	10.04	8.22	7.67
4.5 nm	10.43	9.52	8.46
5.6 nm	10.02	9.76	8.88
(100)-[100] B			
1.9 nm	8.32	6.81	6.95
2.7 nm	8.26	8.27	7.67
3.4 nm	9.35	8.75	8.17
4.5 nm	10.09	9.52	8.60
5.6 nm	10.57	9.76	8.67

with similar accuracy. Figure 5 illustrates the evolution of film conductance with thickness depending on transport direction and local surface environment by showing the transmission per unit area of both structure sets and transport directions with respect to that of bulk copper for increasing film thickness, as computed with DFTB using the custom parameter set.

### B. Transmission pathways

The total transmission coefficients provide information about the total number of electron transmission channels through the films as a whole, while the use of transmission pathways allows for a spatially resolved analysis of charge transport. Transmission pathways calculations have been performed using DFTB with the custom parameter set for both transport orientations of each structure set at the Fermi level  $E_F$ . These localized pathways between individual atom pairs within the thin films enable an extraction of local electron transmission coefficients as a function of depth into the copper films, as shown in Fig. 6. The calculated transmission per unit area near the oxidized surfaces is much lower than at the center of the films, which reveals that the reduction of propagating states caused by the presence of the oxide and its modification of the local electronic structure extends into the film and is not limited to the surface layers. Below the surface oxide layer, transmission per unit area initially increases rapidly with depth and plateaus for distances greater than  $\approx 0.5$  nm away from the surface in structures with (100) surface facets [Fig. 1(a)]; while plateau values are observed for depths greater than  $\approx 0.35$  nm in structures with (110) surface facets [Fig. 1(b)]. This variation in depth up to which the presence of the surface oxide suppresses electron transport is attributed to differences in the local surface environment with varying crystallographic orientations. Values of the transmission per unit area for the thinnest film studied in each structure set (1.9–2.0 nm thick) remain below the maxima seen for the thicker films. With the exception of said films, the depth dependence of the transmission per unit area is remarkably uniform for a given structure set and transport

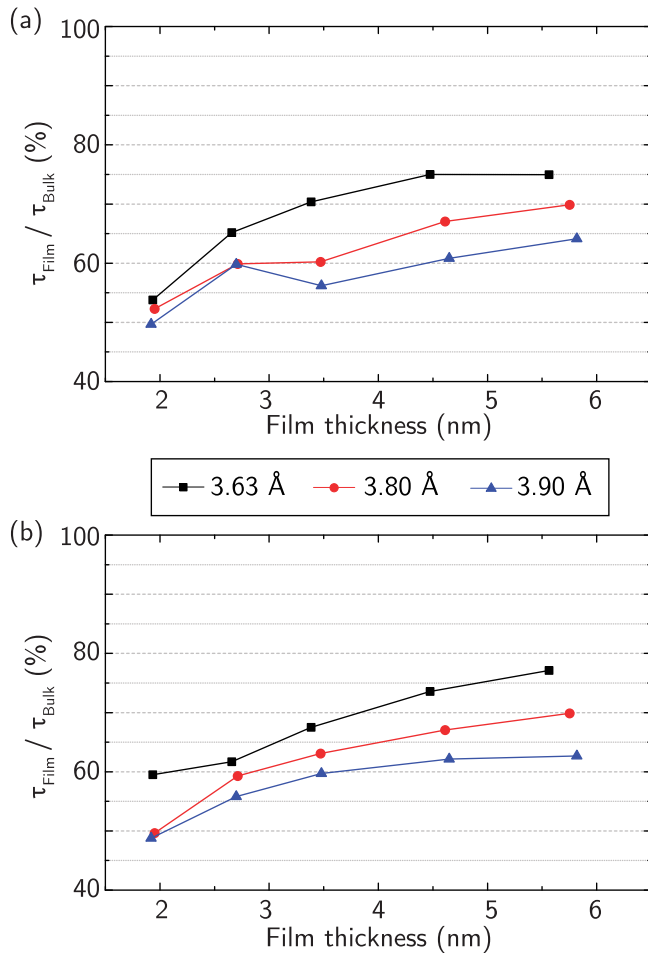


FIG. 3. DFT calculated ratios between the transmission per unit area of structures shown in Fig. 1(a) and bulk Cu. The lengths labeling each curve in the legend indicate the lattice constant (biaxial strain).

direction. A maximum value of transmission per unit area of 50–80% that of bulk copper is reached for depths greater than 0.35–0.5 nm, depending on surface environment and transport direction, in all studied structures thicker than 2 nm, remaining approximately constant all the way through to the center (see Fig. 6). However, these plateau values remain below the full transmission per unit area of bulk copper despite their apparent convergence at the center of the films, an effect brought on by the presence of surface scattering and its limiting of the number of conduction paths for electrons to propagate along the film.

While the center of the films exhibit an atomic structure similar to that of bulk Cu, and hence one may expect the local number of conducting paths to be the same, the close proximity of surfaces imposes restrictions over the number of independent paths in the films, even at the center. The reason behind these differences might be found in the electronic structure of bulk copper: although it exhibits an isotropic conductivity, inspection of the state distribution across its Brillouin zone (BZ) reveals that not all directions are equivalent in terms of states which propagate along them at the Fermi level: While states can be found along  $\Sigma$  and  $\Delta$  associated with [110] and [100] directions, respectively, there are no states along the  $\Lambda$  path—associated with direction [111]—a feature made evident

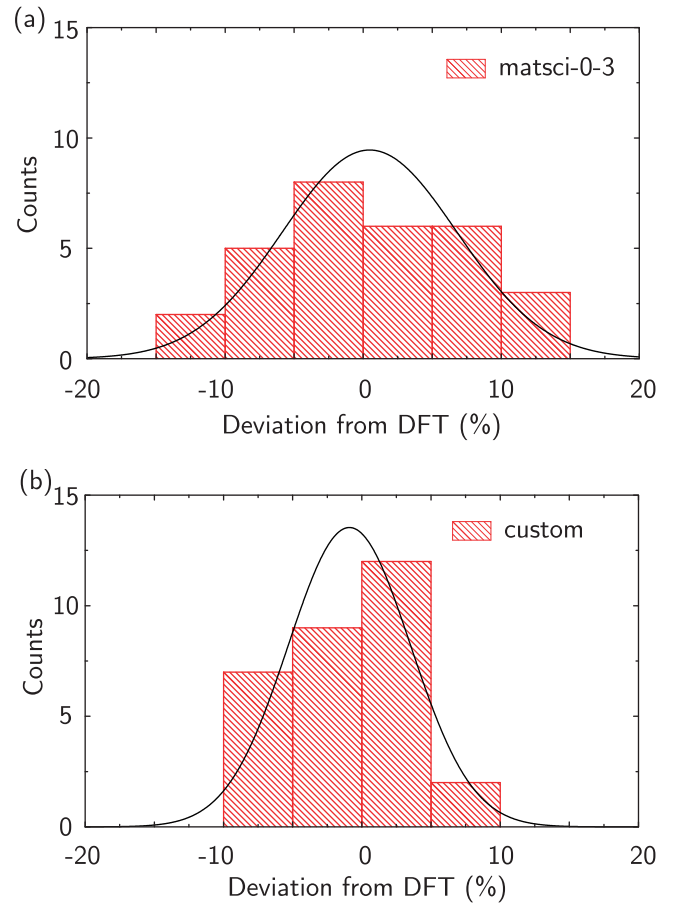


FIG. 4. Histograms showing the error in transmission coefficients obtained using DFTB with respect to DFT transmission at  $E_F$  obtained with (a) matsci, and (b) custom parameter sets. Values for structure set shown in Fig. 1(a) with varying thickness and strain have been compared.

by the shape of the Fermi surface and its vanishing DOS along directions perpendicular to the hexagonal faces of the BZ [49]. It is worth noting that the depth of influence of the surface

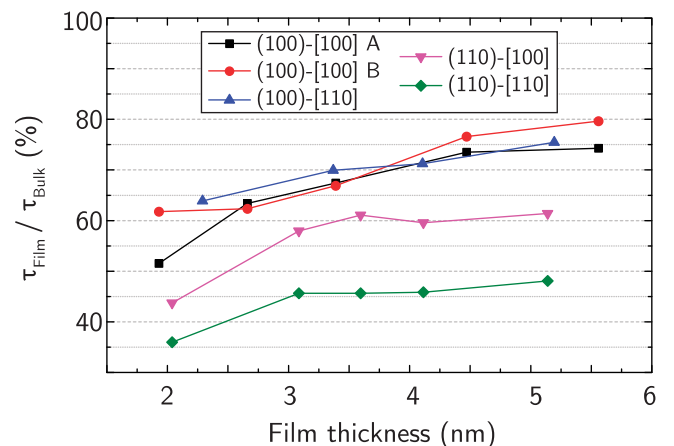


FIG. 5. Evolution of calculated transmission per unit area with film thickness for both structure sets shown in Fig. 1 along the [100] and [110] transport directions. DFTB with the custom parameter set has been employed.

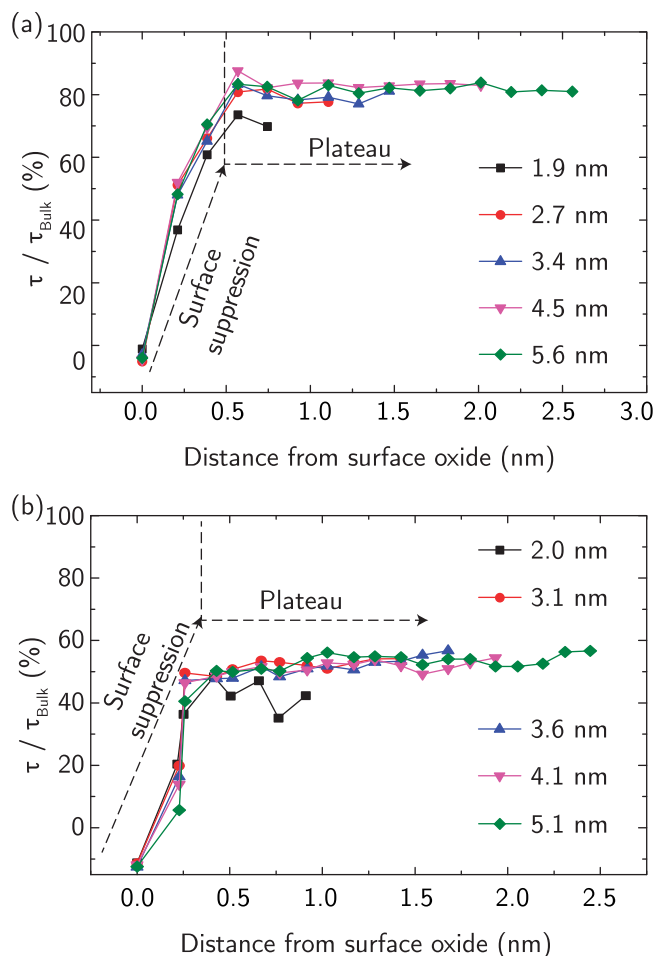


FIG. 6. Transmission per unit area at the Fermi level as a function of distance from the thin film's surface oxide. Transmission is strongly suppressed near films' surfaces, below the surface transmission per unit area initially increases rapidly and plateaus for depths greater than  $\approx 0.35$ – $0.5$  nm, dependent on surface environment.

on electronic transport properties found in this study may be modified when introducing the effects of inelastic sources of scattering and decoherence effects into the model.

### C. Surface scattering model

The previous analysis of the transmission pathways results suggests that the total transmission in all but the thinnest films of each structure set can be decomposed as a sum of two contributions: a *surface* contribution describing transmission for depths less than  $0.35$ – $0.5$  nm into the films and a *plateau* contribution describing transport for greater depths. In terms of transmissions per unit area ( $\tau$ ), we may write:

$$T = A^{\text{Surf}} \tau_{\text{Surf}} + A^{\text{Plat}} \tau_{\text{Plat}}, \quad (5)$$

where we have split the cross-sectional area of the film into the area of the surface and plateau regions, and each term on the rhs is proportional to the maximum current that can flow through the corresponding section of the film. Since the depth up to which transmission is strongly suppressed by the surface does not vary with thickness, we shall consider  $A^{\text{Surf}}$  to be constant for all structures—except the thinnest films—within

TABLE II. Computed values for local transmission per unit area with respect to bulk Cu for both structure sets using the custom DFTB parameter set. Values have been obtained by performing a linear fit of obtained data to Eq. (5); correlation coefficients greater than 0.99 were obtained in all cases. Values shown in parenthesis have been obtained with DFT.

	$\tau_{\text{Surf}}/\tau_{\text{Bulk}}(\%)$	$\tau_{\text{Plat}}/\tau_{\text{Bulk}}(\%)$
(100)-[100] A	38 (54)	85 (77)
(100)-[100] B	19 (23)	97 (88)
(100)-[110]	39	86
(110)-[100]	44	65
(110)-[110]	36	52

each set. We then proceed to fit Eq. (5) in order to obtain values for  $\tau_{\text{Surf}}$  and  $\tau_{\text{Plat}}$  at the Fermi level.

Table II shows the obtained values for transmission per unit area on each region for both structure sets and transport directions, scaled by values obtained for bulk Cu. For the first set of structures, A and B transport directions correspond to bulk [100] deep into the film as asymmetry is only introduced near the surface. It is seen that while the surface environment for electrons propagating along the B axis—in which the missing rows of Cu atoms are parallel to the transport direction—is more resistive, it has less of an impact on the resistance of the plateau region than for electrons traveling along the A axis. This correlates to the fact that total film transmission per unit area increases at a higher rate for transport along the B axis as thickness increases, as can be seen in Fig. 5. In the case of these two transport directions, we have included results obtained with DFT as an assessment of the error introduced by the use of DFTB on the values of fitted parameters: While differences on  $\tau_{\text{Surf}}$  can be as high as 40%, qualitative trends hold and errors on  $\tau_{\text{Plat}}$  remain within the expected 10%.

Results for transport along the [100] crystallographic direction for the second set of structures show its corresponding surface environment's resistance to be similar to that of transport along (100)-[100] A, although it results in a higher resistance at the plateau region, a feature evident in the fact that its transmission per unit area increases less than for structures in the first set in the 3–5 nm thickness range (see Fig. 5). Finally, results for transport along the [110] direction show both surface environments to be similarly resistive, with structures with (110) surface facets exhibiting lower transmission per unit area in the plateau region. Overall, the set of structures with (100) surfaces exhibit stronger anisotropy, as shown by the vertical separation between curves corresponding to both of its transport directions in Fig. 5.

Figure 7 shows a visual representation of transmission pathways crossing a plane perpendicular to the transport direction and located halfway between two atomic planes. Two cases are illustrated: (100)-[100] A and (110)-[110]. Transmission along [100] is shown to always take place at an angle with respect to the transport direction, while transport along [110] is shown to have a sizable parallel component. This is shown by the fact that the largest transmission pathways (bubbles) along [100] are found halfway between Cu atoms (+), while the largest bubbles are found to lay directly

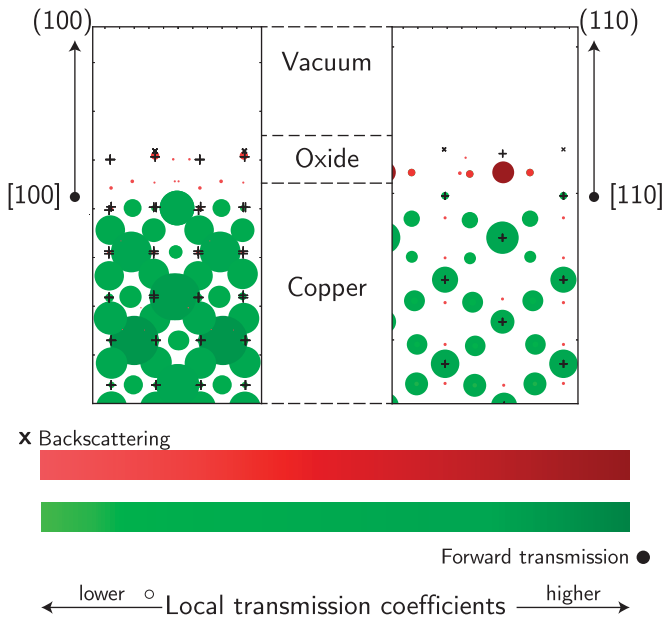


FIG. 7. Projections of transmission pathways at the Fermi level at a plane perpendicular to the transport direction and located halfway between atomic planes. Both the size of the bubbles and their color represent the magnitude of each pathway. Cu atoms are represented by + signs, while O atoms at the surface are shown as x. Transport along direction A of the structure shown in Fig. 1(a) is shown on the left; while the plot on the right corresponds to transport along [110] in the structure shown in Fig. 1(b).

on top of Cu atoms for transport occurring along [110]. Forward transmission is found to be severely suppressed when approaching both surfaces, with an associated increase in backscattering coefficients.

#### IV. CONCLUSIONS

It is found that the DFTB calculations of electron transmission performed provide a reasonable approximation to DFT for Cu/O systems, with the custom parameter set performing

closer to DFT (error <10%) when compared to the matsci set (error <13%). This enables the calculation of transport properties of structures with a larger number of atoms and hence more realistic models of nanoscale interconnects. It is found that oxidation of the surface of copper thin films results in a dramatic reduction of electron transmission directly at the interface, an effect which severely degrades local electron transmission coefficients for distances of up to approximately 0.35–0.5 nm into the films, depending on the crystallographic orientation of exposed surface facets—a result which highlights the importance and provides a scale length for interface effects in nanoscale copper systems—although introducing the effects of inelastic scattering and other decoherence effects might modify surface effects’ depth of influence discussed in this paper. Maximizing conductance in nanoscale copper interconnects requires careful interface design between conductor and barrier layer as the chemical environment at the surface and orientation along which transport occurs can have critical impact for Cu systems with feature lengths below 10 nm. Tensile strain tends to be detrimental to film conductance as the transmission per unit area is found to be reduced for films under biaxial tensile strain studied in this paper. For film thicknesses of  $\approx 3$  nm and greater, a core region for which transmission is somewhat independent of depth is formed, although bulklike transmission has not been observed even at the center of films as thick as 5.6 nm. The use of a localized transmission model shows the resistance of the studied films to dramatically increase near the surface; whereas the increase in resistance at the core region is found to strongly depend on the surface environment and transport direction.

#### ACKNOWLEDGMENTS

This work was performed as part of the Intel-Tyndall research collaboration sponsored by Intel Components Research. A.S.S. was funded under an Irish Research Council postgraduate scholarship. Partial funding was provided by the Science Foundation Ireland Investigator program, Grant No. 13/IA/1956. We are grateful to QuantumWise A/S for support and access to the QuantumWise simulation software. Atomistic visualizations were rendered using VESTA [50].

- [1] W. Steinhögl, G. Schindler, G. Steinlesberger, and M. Engelhardt, *Phys. Rev. B* **66**, 075414 (2002).
- [2] W. Zhang, S. H. Brongersma, Z. Li, D. Li, O. Richard, and K. Maex, *J. Appl. Phys.* **101**, 063703 (2007).
- [3] K. Fuchs, *Math. Proc. Cambridge Philos. Soc.* **34**, 100 (1938).
- [4] A. F. Mayadas and M. Shatzkes, *Phys. Rev. B* **1**, 1382 (1970).
- [5] D. Josell, S. H. Brongersma, and Z. Tokei, *Annu. Rev. Mater. Res.* **39**, 231 (2009).
- [6] R. Henriquez, S. Cancino, A. Espinosa, M. Flores, T. Hoffmann, G. Kremer, J. G. Lisoni, L. Moraga, R. Morales, S. Oyarzun, M. A. Suarez, A. Zúñiga, and R. C. Munoz, *Phys. Rev. B* **82**, 113409 (2010).
- [7] R. Henriquez, M. Flores, L. Moraga, G. Kremer, C. Gonzalez-Fuentes, and R. C. Munoz, *Appl. Surf. Sci.* **273**, 315 (2013).
- [8] T. Sun, B. Yao, A. P. Warren, K. Barmak, M. F. Toney, R. E. Peale, and K. R. Coffey, *Phys. Rev. B* **79**, 041402 (2009).
- [9] T. Sun, B. Yao, A. P. Warren, K. Barmak, M. F. Toney, R. E. Peale, and K. R. Coffey, *Phys. Rev. B* **81**, 155454 (2010).
- [10] J. S. Chawla and D. Gall, *Appl. Phys. Lett.* **94**, 252101 (2009).
- [11] J. S. Chawla, F. Gstrein, K. P. O’Brien, J. S. Clarke, and D. Gall, *Phys. Rev. B* **84**, 235423 (2011).
- [12] J. S. Chawla, F. Zahid, H. Guo, and D. Gall, *Appl. Phys. Lett.* **97**, 132106 (2010).
- [13] F. Zahid, Y. Ke, D. Gall, and H. Guo, *Phys. Rev. B* **81**, 045406 (2010).
- [14] S. M. Rosnagel and T. S. Kuan, *J. Vac. Sci. Technol. B* **22**, 240 (2004).
- [15] P. Y. Zheng, R. P. Deng, and D. Gall, *Appl. Phys. Lett.* **105**, 131603 (2014).

- [16] H. Zeng, R. McFarlane, and K. Mitchell, *Surf. Sci.* **208**, L7 (1989).
- [17] A. Atrei, U. Bardi, G. Rovida, E. Zanazzi, and G. Casalone, *Vacuum* **41**, 333 (1990).
- [18] M. Kittel, M. Polcik, R. Terborg, J.-T. Hoefl, P. Baumgrtel, A. Bradshaw, R. Toomes, J.-H. Kang, D. Woodruff, M. Pascal, C. Lamont, and E. Rotenberg, *Surf. Sci.* **470**, 311 (2001).
- [19] N. Bonini, A. Kokalj, A. D. Corso, S. de Gironcoli, and S. Baroni, *Surf. Sci.* **600**, 5074 (2006).
- [20] M. J. Harrison, D. P. Woodruff, J. Robinson, D. Sander, W. Pan, and J. Kirschner, *Phys. Rev. B* **74**, 165402 (2006).
- [21] X. Duan, O. Warschkow, A. Soon, B. Delley, and C. Stampfl, *Phys. Rev. B* **81**, 075430 (2010).
- [22] M. Z. Baykara, M. Todorović, H. Mönig, T. C. Schwendemann, O. Ünverdi, L. Rodrigo, E. I. Altman, R. Pérez, and U. D. Schwarz, *Phys. Rev. B* **87**, 155414 (2013).
- [23] S. L. T. Jones, A. Sanchez-Soares, J. J. Plombon, A. P. Kaushik, R. E. Nagle, J. S. Clarke, and J. C. Greer, *Phys. Rev. B* **92**, 115413 (2015).
- [24] F. Besenbacher and J. K. Nørskov, *Prog. Surf. Sci.* **44**, 5 (1993).
- [25] Y. Uehara, T. Matsumoto, and S. Ushioda, *Phys. Rev. B* **66**, 075413 (2002).
- [26] S. Kishimoto, M. Kageshima, Y. Naitoh, Y. J. Li, and Y. Sugawara, *Surf. Sci.* **602**, 2175 (2008).
- [27] Y. J. Li, S. H. Lee, Y. Kinoshita, Z. M. Ma, H. Wen, H. Nomura, Y. Naitoh, and Y. Sugawara, *Nanotechnology* **27**, 205702 (2016).
- [28] J. Bamidele, Y. Kinoshita, R. Turanský, S. H. Lee, Y. Naitoh, Y. J. Li, Y. Sugawara, I. Štich, and L. Kantorovich, *Phys. Rev. B* **86**, 155422 (2012).
- [29] J. Bamidele, S. H. Lee, Y. Kinoshita, R. Turanský, Y. Naitoh, Y. J. Li, Y. Sugawara, I. Štich, and L. Kantorovich, *Nat. Commun.* **5**, 4476 (2014).
- [30] J. Bamidele, Y. Kinoshita, R. Turanský, S. H. Lee, Y. Naitoh, Y. J. Li, Y. Sugawara, I. Štich, and L. Kantorovich, *Phys. Rev. B* **90**, 035410 (2014).
- [31] [www.openmx-square.org](http://www.openmx-square.org).
- [32] Atomistix ToolKit version 2014-1 QuantumWise A/S, [www.quantumwise.com](http://www.quantumwise.com).
- [33] M. Brandbyge, J.-L. Mozos, P. Ordejón, J. Taylor, and K. Stokbro, *Phys. Rev. B* **65**, 165401 (2002).
- [34] J. M. Soler, E. Artacho, J. D. Gale, A. Garcia, J. Junquera, P. Ordejón, and D. Sanchez-Portal, *J. Phys.: Condens. Matter* **14**, 2745 (2002).
- [35] J. P. Perdew, K. Burke, and M. Ernzerhof, *Phys. Rev. Lett.* **77**, 3865 (1996).
- [36] I. Morrison, D. M. Bylander, and L. Kleinman, *Phys. Rev. B* **47**, 6728 (1993).
- [37] T. Ozaki, *Phys. Rev. B* **67**, 155108 (2003).
- [38] T. Ozaki and H. Kino, *Phys. Rev. B* **69**, 195113 (2004).
- [39] H. J. Monkhorst and J. D. Pack, *Phys. Rev. B* **13**, 5188 (1976).
- [40] R. Landauer, *IBM J. Res. Dev.* **1**, 223 (1957).
- [41] S. Datta, *Electronic Transport in Mesoscopic Systems* (Cambridge University Press, Cambridge, UK, 1995).
- [42] <http://www.dftb.org>.
- [43] N. Jardillier, Ph.D. thesis, Université Montpellier II, Montpellier, 2006.
- [44] G. Seifert, D. Porezag, and T. Frauenheim, *Int. J. Quantum Chem. Quantum* **58**, 185 (1996).
- [45] G. Seifert and J.-O. Joswig, *Wiley Interdisciplinary Reviews: Computational Molecular Science* **2**, 456 (2012).
- [46] J. C. Slater and G. F. Koster, *Phys. Rev.* **94**, 1498 (1954).
- [47] M. Wahiduzzaman, A. F. Oliveira, P. Philippsen, L. Zhechkov, E. van Lenthe, H. A. Witek, and T. Heine, *J. Chem. Theory Comput.* **9**, 4006 (2013).
- [48] G. Solomon, C. Herrmann, T. Hansen, V. Mujica, and M. Ratner, *Nat. Chem.* **2**, 223 (2010).
- [49] B. Segall, *Phys. Rev.* **125**, 109 (1962).
- [50] K. Momma and F. Izumi, *J. Appl. Crystallogr.* **44**, 1272 (2011).